



Corrosion susceptibility and mechanical properties of friction-stir-welded AA2024-T3 joints

Na Li^{1,2} · Yaxin Xu¹ · Wenya Li¹ · Pengliang Niu³ · Achilles Vairis^{1,4}

Received: 9 December 2021 / Accepted: 21 February 2022 / Published online: 5 March 2022
© International Institute of Welding 2022

Abstract

The joining of AA2024-T3 with friction stir welding (FSW) at a rotational speed of 600 rpm and welding speed of 200 mm/min produces areas with significantly different heterogeneous microstructures, which relate to mechanical properties and corrosion behavior. In this study, the mechanical properties and corrosion susceptibility of different zones of an AA2024-T3 joint were investigated with tensile, hardness, and electrochemical testing. The joint was found to have reduced mechanical properties compared to base metal due to the significant microstructural changes. The developing localized high temperatures allow re-formation of the Guinier–Preston–Bagaryatsky (GPB) zone and dissolution of S phase, resulting in lowers hardness in the stir zone (SZ). Tensile test specimens failed in the lowest hardness area located in the heat-affected zone (HAZ) at the retreating side (RS). The SZ exhibited a relatively low pitting corrosion resistance compared to that of the BM and HAZ of the top surface, due to the refined grains and a larger number of intermetallic particles during welding.

Keywords Friction stir welding · Aluminum alloy · Mechanical properties · Corrosion sensitivity

1 Introduction

When using conventional fusion welding techniques, such as gas tungsten arc welding (GTAW) and gas metal arc welding (GMAW) high-strength aluminum alloys, joints develop porosity, poor dendritic solidification microstructures, and reduced mechanical properties [1–3]. So, a solid-state

joining technique like friction stir welding (FSW) can join high-strength alloys which belong to the 2xxx and 7xxx series [4, 5], which alloys' joints always contain welding defects when welded with conventional fusion techniques [6, 7], while FSW produces joints without defects with the added advantages of refining the microstructure, decreasing the grain size and improving the tensile properties, hardness, and fatigue life. However, these joints undergo intense frictional heating and plastic deformation as a rotating tool is plunged into the joint [1, 8, 9]. These effects may make the joint more susceptible to corrosion than the base material itself. There exist four microstructural zones in the FSW joint: stir zone (SZ), thermomechanically affected zone (TMAZ), heat-affected zone (HAZ), and base material (BM) [4, 10]. Due to the heterogeneous heating and deformation along the joint, these zones have different microstructures (in terms of grain size, dislocation structure/density, precipitate state, etc.). Furthermore, the microstructures in the advancing side (AS) and that in the retreating side (RS) are asymmetric due to the inherent characteristics of the process [11–13], so it is expected that they will exhibit different degrees of corrosion resistance and micromechanical properties.

During service, it is expected that FSW joints will be exposed to various corrosive environments. In the past

Recommended for publication by Commission III-Resistance Welding, Solid State Welding, and Allied Joining

✉ Yaxin Xu
xu.yaxin@nwpu.edu.cn

✉ Wenya Li
liwy@nwpu.edu.cn

- ¹ State Key Laboratory of Solidification Processing, Shaanxi Key Laboratory of Friction Welding Technologies, Northwestern Polytechnical University, Xi'an 710072, People's Republic of China
- ² Shaanxi Railway Institute, Weinan 714000, Shaanxi Province, People's Republic of China
- ³ School of Aeronautical Manufacturing Engineering, Nanchang Hangkong University, 696 Fenghe South Road, Nanchang, People's Republic of China
- ⁴ Mechanical Engineering Department, Hellenic Mediterranean University, 71004 Heraklion, Crete, Greece

decade, a number of published works have focused on microstructural evolution [14, 15], mechanical properties [1, 16, 17], residual stress analysis [18, 19], and numerical simulation of the plastic deformation and temperature field [20, 21] of such joints. However, there are no publications investigating the relationship between microstructure, mechanical properties, and corrosion behavior of aluminum alloys FSW joints. It is an established fact that precipitates and second-phase particles play an important role in corrosion behavior in the case of heat-treatable aluminum alloys. Zhang et al. [1] examined the hardness profiles and microtensile properties with the microstructure in 2024-T3 which had been joined with FSW. It was found that lower hardness and tensile properties were measured in the SZ and HAZ and the lower mechanical properties were associated with the dissolution of the GPB zone and the coarsening of S phase during the thermal cycle and localized plastic flow of the process. Jariyaboon et al. [21] reported that both SZ and HAZ in the AA2024-T351 joints are susceptible to corrosion. The SZ shows a larger cathodic activity than the HAZ due to the increased number of intermetallic compound particles. All of the joints produced fractured in the lowest hardness area in the HAZ where partial dissolution of the GPB zone and coarsening of the S phase occur. Xu et al. [22] identified that the state of the precipitate and second particle strongly relate to the corrosion performance of the joint along its thickness and the hardness measured through the joint for the 2219-O aluminum alloy. It is expected that FSW joints are more sensitive to the corrosion environment than the Al matrix itself in the case of high-strength Al alloys [23]. The mechanical properties and corrosion behavior are affected by grain size, precipitation distribution, and size, as well as intermetallic phases present.

It has been established that in order to prevent corrosion, the surfaces of the 2xxx or 7xxx series aluminum alloys need to have pure aluminum (of about 30 μm thickness) cladding [1, 20]. This layer is destroyed during FSW, which removes the corrosion protection from the top surface of the joint. As corrosion usually attacks a joint on the top surface, the study of the top surface is required [24]. There is however limited literature on the investigation of corrosion behavior on the top surface of FSW joint, which is required for the assessment of service properties of such joints. Hence, the objective of this work is to measure mechanical properties (microhardness and tensile properties), identify microstructure evolution (precipitation distribution), and measure corrosion susceptibility of the top surface under optimum welding parameters. A relationship between microstructure,

microhardness, and corrosion performance of 2024-T3 joint was established, because of its wide industrial use.

2 Experimental procedure

2.1 Materials

The 3.2-mm-thick plate of commercial AA2024-T3 aluminum alloy was used as base material in this study, with its composition shown in Table 1. The specimens had dimensions 200 mm \times 90 mm \times 3.2 mm, and they were butt welded with a Beijing FSW Technology Co., Ltd. of Beijing, FSW machine. The welding direction was parallel to the rolling direction of the sheets along the sheet length of 200 mm. The AA2024-T3 sheets were cleaned with acetone prior to welding and were fixed tightly using a custom fixture. The friction stir tool material was H13 tool steel. The tool shoulder was concave with a diameter of 10 mm, and the tool pin is a right-hand threaded conical probe of 3.4 mm in diameter and 2.9 mm in length. The tool tilt angle was set at 2.5° (Z-axis) and the plunging depth at 0.2 mm. In addition, the optimum welding parameters were set to, following tests, a rotational speed of 600 rpm and traveling speed of 200 mm/min [25].

2.2 Test methods

The metallographic images of the cross section of the joint and the corrosion depth were obtained with an optical microscope (OM) from samples embedded in resin, which were progressively ground with SiC abrasive papers from P200 up to P5000 size, and polished with 1.5 μm diamond paste then to be etched with Dix-Keller's reagent [26]. A scanning electron microscope (SEM) was used to characterize the corrosion morphologies and tensile fracture surfaces. Differential scanning calorimetry (DSC) was used to identify the precipitation evolution of the joint with measurements conducted in Ar atmosphere to minimize oxidation. The area of TMAZ is narrowest among other zones, and the DSC sample is not extracted in TMAZ. In this study, the DSC sample was $\varnothing 4 \times 2$ mm. DSC experiments were also carried out at a heating rate of 10 °C/min in the temperature range of 50 to 450 °C. Tensile testing was performed at room temperature at a displacement rate of 1 mm/min with specimens, which were machined in a direction perpendicular to the joint and a gauge length of 25 mm. The specimens were cut from the welded sheets with electric discharge machining, as shown in Fig. 1.

Table 1 Chemical composition of AA2024 alloy (wt%)

| Cu | Mg | Mn | Fe | Si | Cr | Zn | Ti | Others | Al |
|---------|---------|---------|------------|------------|------------|-------------|-------------|-------------|-----|
| 3.8~4.9 | 1.2~1.8 | 0.3~0.9 | ≤ 0.5 | ≤ 0.5 | ≤ 0.1 | ≤ 0.25 | ≤ 0.15 | ≤ 0.15 | Bal |

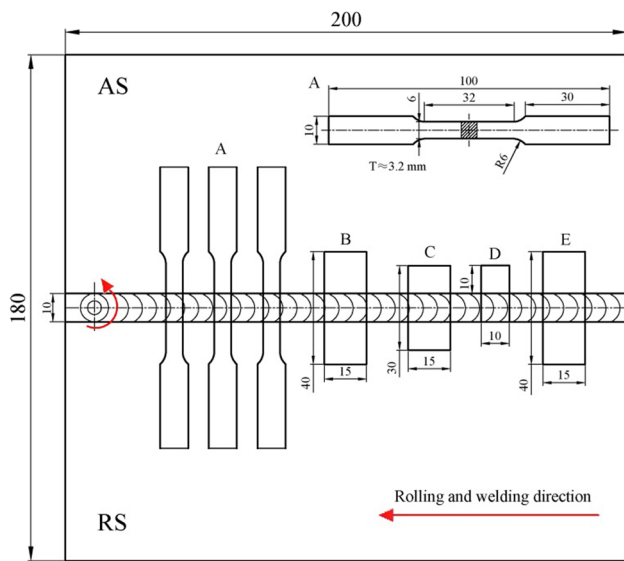


Fig. 1 Position and detail of samples (A, tensile specimen; B, metallographic specimen; C, hardness specimen; D, DSC specimen; E, electrochemical corrosion testing specimen; mm)

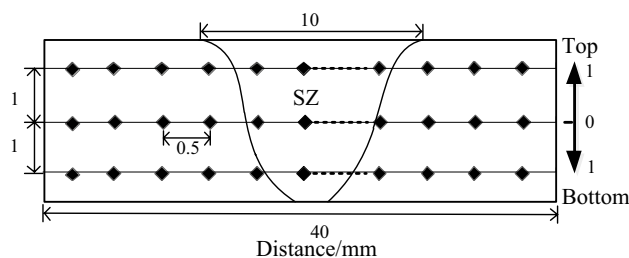


Fig. 2 Positions of microhardness measurements

Vickers hardness was measured across the cross-sectional surface for a load of 200 g applied for 15 s. As shown in Fig. 2, three series of measurements were taken across the weld (BM, HAZ, TMAZ, SZ) at a spacing of 0.5 mm of each other. The width of the measured zone is 40 mm while being at 0.5 mm off the top and bottom surfaces of the joint. The three series of hardness measurements were performed and classified as: center line of the cross section (L1), top 1 mm (L2), and bottom 1 mm (L3) and shown in the figure. Each line of the series of measurements incorporated 80 measurements that extended from the center away up to 20 mm on both the retreating side (RS) and the advancing side (AS).

In order to relate microhardness and tensile strength measurements with changes in corrosion susceptibility within the joint, localized electrochemical measurements were made on the top surface of the joint (Fig. 1) using the three-electrode system. The reference electrode was saturated calomel electrode (SCE) with Luggin capillary, while the counter electrode was a large platinum sheet and the

working electrode was the joint itself with an approximate area of 0.2 cm^2 . Prior to electrochemical measurements, specimens were mechanically ground and polished to mirror surface finish, washed with distilled water, and dried in warm air. The test solution used was a non-deaerated and unstirred 3.5 wt% NaCl aqueous solution at ambient temperature. An equal volume of the same concentration fresh testing solution was provided to each specimen. Tafel polarization scans were conducted, which started with a range of -0.25 V vs open circuit potential (OCP) up to 0.25 V vs OCP at a scan rate of 0.167 mV/s . Electrochemical impedance spectroscopy (EIS) was carried out at voltage amplitude of $\pm 5 \text{ mV}$ in the 0.01 to 100 kHz range[27].

3 Results and discussion

3.1 Microstructure

Figure 3 shows the metallographic images of grain size and shape distribution of the weld cross section in each weld zone when welding with rotation speed of 600 rpm and traveling speed of 200 mm/min. The average grain size and shape from BM to HAZ and SZ change as shown in Fig. 1b–d, due to the different temperatures and plastic deformation locally experienced during welding. It can be seen that the microstructure of BM has highly elongated grains of $20\sim 40 \mu\text{m}$ length and $3\sim 5 \mu\text{m}$ width. The HAZ, also exposed to the same temperature history, has the same microstructure as BM with more elongated grains. It can be established that TMAZ undergoes less intense mechanical stirring action and has upward directed grains, which are slightly elongated and bent along the rotation direction [28]. The TMAZ is quite narrow, making it difficult to take electrochemical measurements, as it barely extends to the top weld surface. In these welds no recrystallization observed in TMAZ. The SZ consists of relatively fine, equiaxed grains, with an average size of $3 \mu\text{m}$, as dynamic recrystallization occurred under the intense deformation and frictional heating present.

Figure 4 shows back-scattered electron microscope images of the intermetallic particle distribution in all regions of the joint, as it has been established that the distribution of secondary phases can affect localized corrosion resistance [21, 22]. Coarse white intermetallic particles are present in all three microstructural areas, whose distribution and size is controlled by plastic deformation. These intermetallics were of two types of particles [22, 29, 30]: small round-shaped S-phase (Al_2CuMg) and irregularly shaped Fe and Si enriched residual impurity particles (the corresponding EDS measurement has not been included), both of which are usually found in such areas. The size of the intermetallics was attributed to two factors: (i) During FSW the

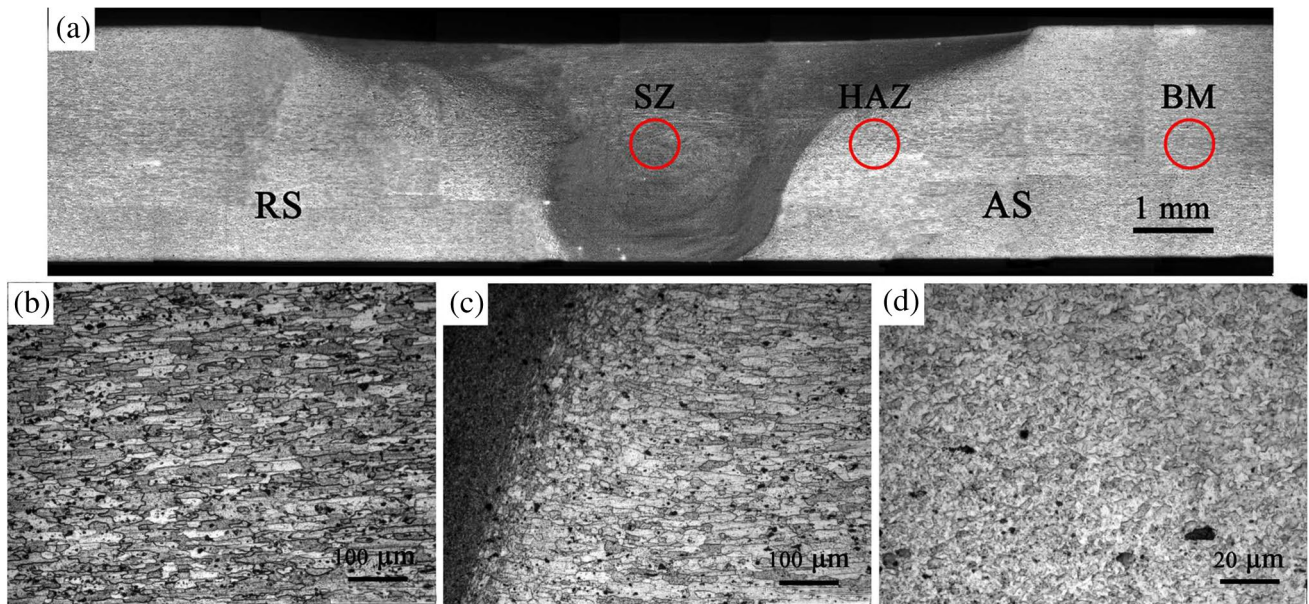
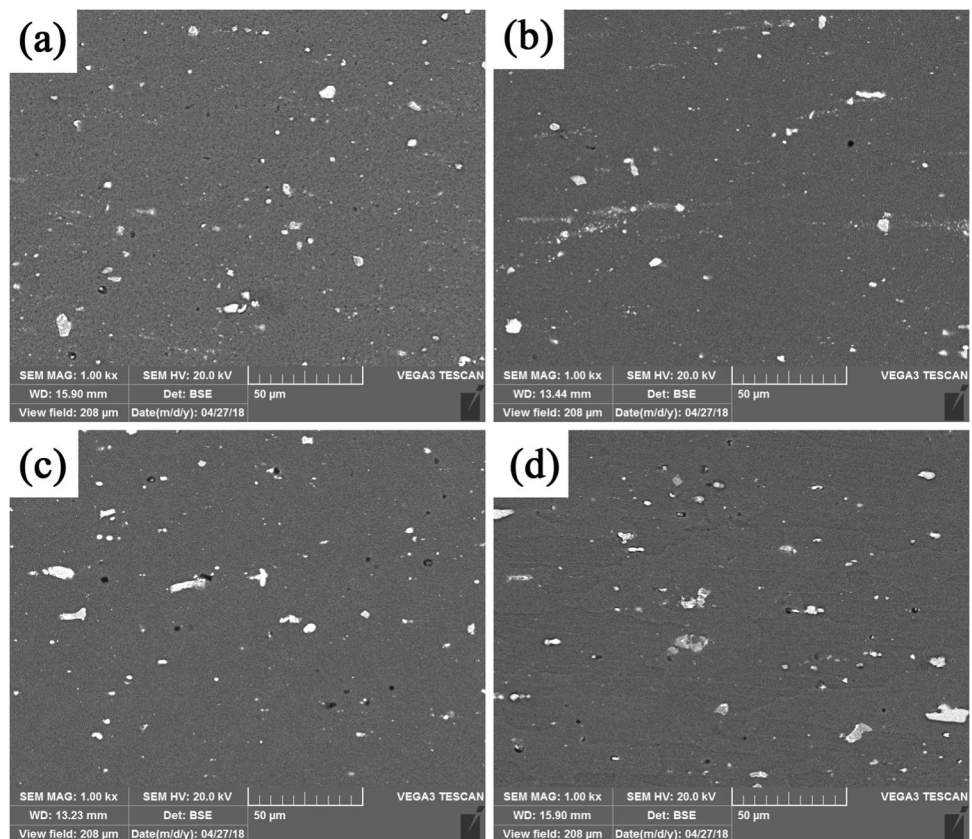


Fig. 3 Cross section of FSWed AA2024-T3 joint: (a) global view, (b) BM, (c) TMAZ, and HAZ in the AS and (d) SZ

Fig. 4 Backscattered scanning electron observations of intermetallic distribution: (a) SZ, (b) TMAZ, (c) HAZ, and (d) BM



AA2024 alloy, the intermetallics are broken up due to the stirring action (mainly plastic deformation). And the larger the stirring action is, the smaller the intermetallics are. The gradual decrease in the size of intermetallics and increase in

number is due to the intense change in plastic deformation from BM, HAZ, and TMAZ to SZ. (ii) The intermetallics were dissolved and re-precipitated under the action of phase transformation due to the heat input. These particles cannot

be eliminated and dissolve with heat treatment, but can be grouped together or even eliminated by plastic deformation [21], effects which are typically found in FSW. Particles both in BM and HAZ appear the same to these intermetallic particles (Fig. 4a and b). The intermetallics in the TMAZ were redistributed along the rotation direction due to the effect of the rotating pin (Fig. 4c). However, intermetallics in the SZ show a uniform size and distribution due to intense stirring and mixing (Fig. 4d).

3.2 Microhardness map and differential scanning calorimetry curves

Figure 5 shows the hardness profiles in the top, middle, and bottom of weld cross section, where the lower hardness

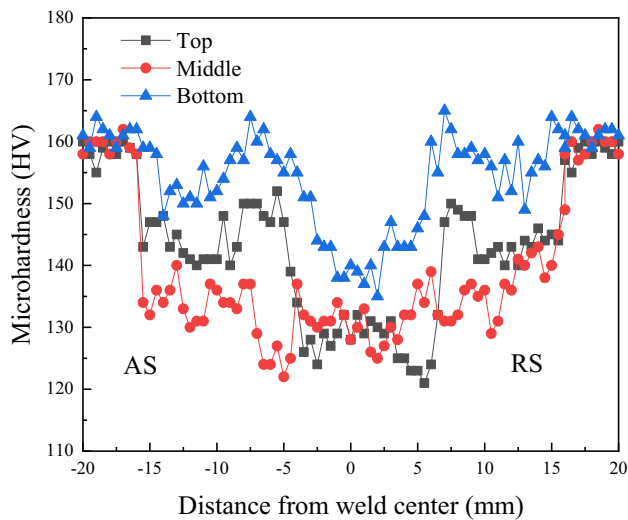


Fig. 5 Hardness profiles in the top, middle, and bottom of cross section of the joint

areas are located in the SZ and HAZ of the RS and AS. The width of the soft zone is about 30 mm, which is the ratio that has been observed in literature [31–33]. The hardness distribution is different in the top, middle, and bottom of weld cross section, due to the heterogeneous heat input during welding. This could be attributed to the following: grain size and precipitated phase are obviously heterogeneous in top, middle, and bottom cross sections. Microhardness is affected strongly by the strengthening precipitates of the Guinier–Preston–Bagaryatsky (GPB) zones and S phase (Al_2CuMg) [29, 33, 34].

The DSC is a reliable and powerful tool to investigate solid-state reactions in precipitation strengthened Al alloys like the 2xxx series Al alloys, and that of AA2024 consists of GPB and S phase [34]. Figure 6a shows the DSC curves of BM, HAZ, and SZ. According to the literature [34], a well-defined endothermic peak A corresponds to the dissolution of GPB zone, and the exothermic peak B can be linked to the precipitation of S phases from the solid solution resulting from the dissolution of the GPB zone. The following equations proposed by Genevois et al. [6] were used in this study to calculate the relative fractions of GPB zone (f_{GPB}) and S phases (f_S) originally present in the sample.

Figure 6a shows the DSC curves of BM, HAZ, and SZ, where an endothermic peak A is shown between 170 and 240 °C with maximum at ~225 °C, due to the dissolution of GPB zone from solute clusters (mainly Cu-Mg clusters) [1]. As dissolution is observed in all three zones, it is understood that GPB zone exists. The exothermic peak B is shown between ~230 and 300 °C, and it is associated with the precipitation of S phases from the solid solution and, in addition, it is the effect of the dissolution of the GPB zone. It can be assumed that the peak area A is S_A and S_{A0} with a volume fraction of f_{GPB} , and the peak B is S_B and S_{B0} with a volume fraction of f_S . According to [34], the relative ratios

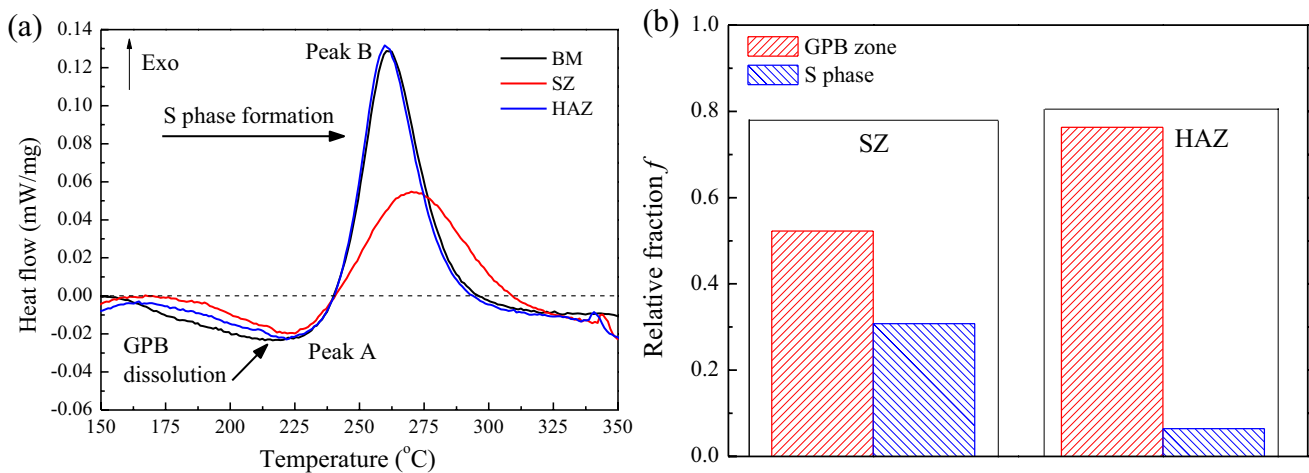


Fig. 6 DSC results. (a) DSC thermograms of BM, SZ, and HAZ. (b) Relative fractions of GPB zones and S phases

of the GPB zone (f_{GPB}) and the S phase (f_S) which were initially present in the joint can be estimated by the following:

$$f_{GPB} = \frac{S_A}{S_{A0}} \quad (1)$$

$$f_S = 1 - \frac{S_B}{S_{B0}} \quad (2)$$

3.3 Tensile properties and fracture surfaces

Figure 7a and b show the stress–strain curves and test results for both BM and the joint, where error bars in Fig. 7b indicate the range of test results for three specimens per case. There were no defects in the weld due to insufficient heat input. However, the ultimate tensile strength (UTS), the yield tensile strength (YS), and the elongation (El) of the joint were lower than those of BM. This is related to the

following: at the beginning, during welding, all zones in the joint experience intense heat input and plastic deformation, which result in heterogeneous microstructures and lower mechanical properties [1, 4]. Furthermore, the non-uniform distribution and size of precipitation (S phase, etc.) weaken mechanical properties to a limited extent [1, 4].

In addition, tensile test samples fractured at the HAZ of the RS (inserted figure in Fig. 7a), in which fracture site was related to the weakest zone, i.e., the lowest hardness distribution as shown in Fig. 5. Examination of the fracture surfaces by SEM is shown in Fig. 7c and d, which show tearing ridges and deep dimples (Fig. 7d), characteristics of ductile fracture.

3.4 Electrochemical corrosion

Figure 8 shows the Tafel polarization curves of SZ, HAZ, and BM specimens in a 3.5-wt% NaCl solution where all curves follow the same trend. Electrochemical parameters

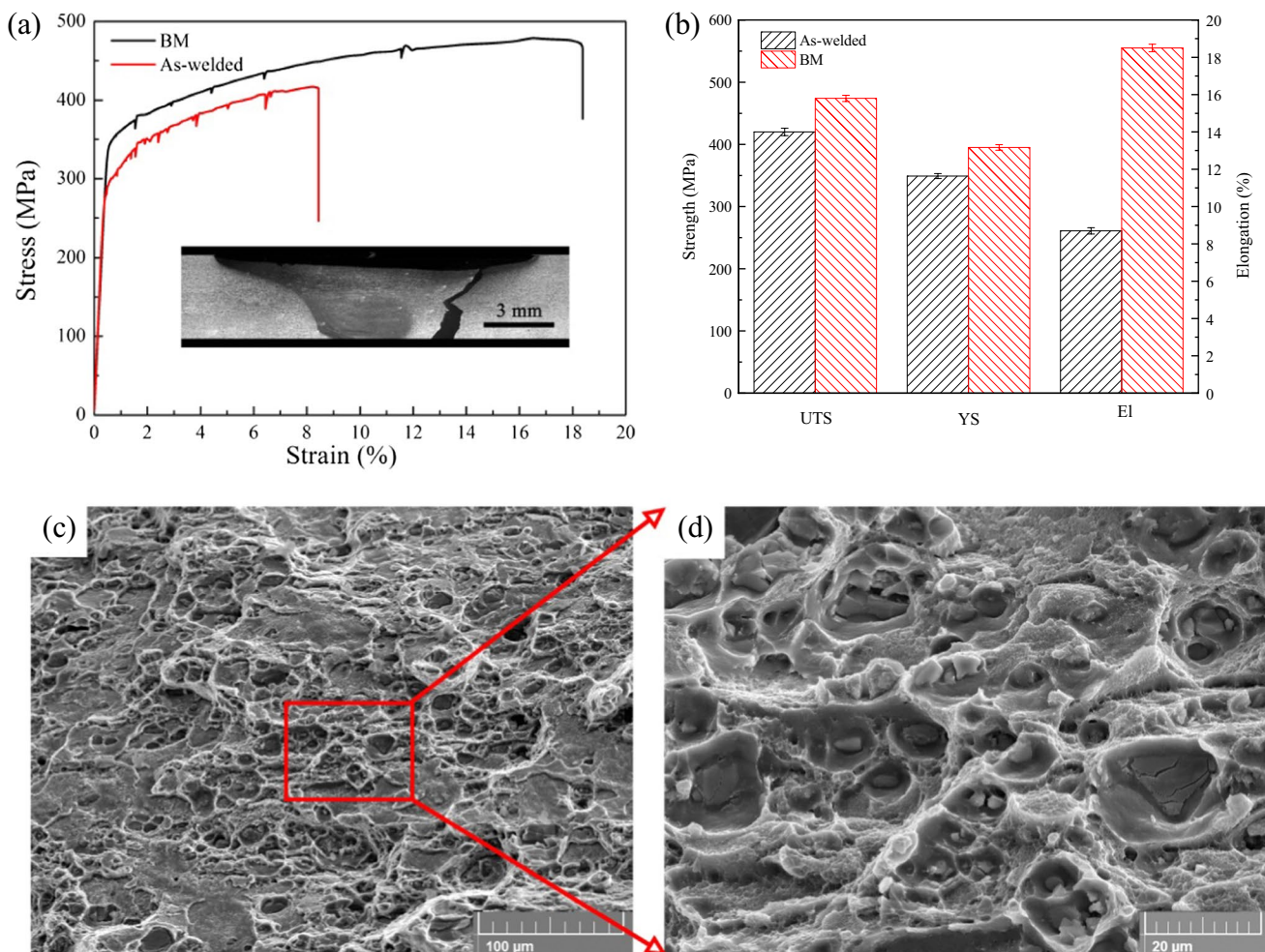


Fig. 7 (a) Stress–strain curves and macrograph of the fractured parts (insert), (b) results of tensile test, (c) fracture surfaces of FSWed joint, and (d) details of fracture surfaces

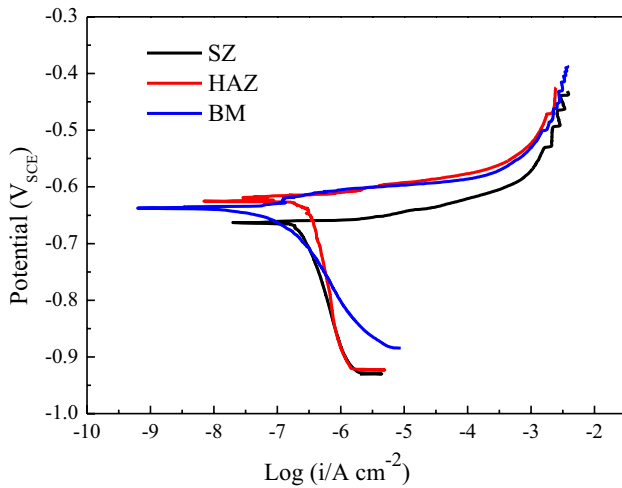


Fig. 8 Tafel polarization curves of the SZ, HAZ, and BM in a 3.5-wt% NaCl solution

Table 2 Electrochemical parameters estimated from the Tafel polarization curves

| Sample | E_{corr} (vs SCE)/mV | i_{corr} (mA/cm ²) |
|--------|-------------------------------|---|
| SZ | -650.2 | 50.9 |
| HAZ | -630.2 | 42.2 |
| BM | -617.6 | 41.9 |

calculated from Tafel polarization curves are shown in Table 2 using linear extrapolation. The corrosion resistance of every zone can be evaluated with these parameters. It can be seen that the corrosion potential (E_{corr}) of the SZ was slightly lower than that of the BM and HAZ, and the corrosion current density (i_{corr}) of the SZ was slightly higher. Furthermore, both HAZ and SZ showed a lower E_{corr} value and higher i_{corr} value than that of the BM. As a result of this, both SZ and HAZ specimens showed an increased tendency for corrosion in the electrochemical Tafel polarization tests, and SZ showed the worst corrosion resistance among three specimens.

EIS measurements were performed in a 3.5-wt% NaCl solution to assess the electrochemical corrosion resistance of SZ, HAZ, and BM. The experimental and fitted Nyquist plots of three specimens are shown in Fig. 9. The Nyquist plots were analyzed using the equivalent electrical circuit and inserted in Fig. 9, where R_s stands for the electrolyte resistance of 3.5 wt% NaCl solution, R_2 represents the resistance of oxide film, R_1 corresponds to the resistance inside the film pores, and Q includes the pseudocapacitance of the film, expressed with the constant phase element (CPE), where C stands for the double layer capacity and R_2 is the main polarization resistance and can directly reveal the corrosion rate. The variation of oxide film resistance (R_2)

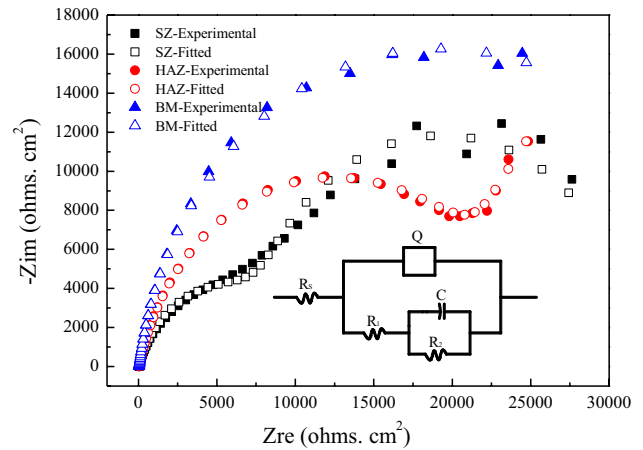


Fig. 9 Nyquist plots and the equivalent circuit diagram of the SZ, HAZ, and BM in a 3.5-wt% NaCl solution

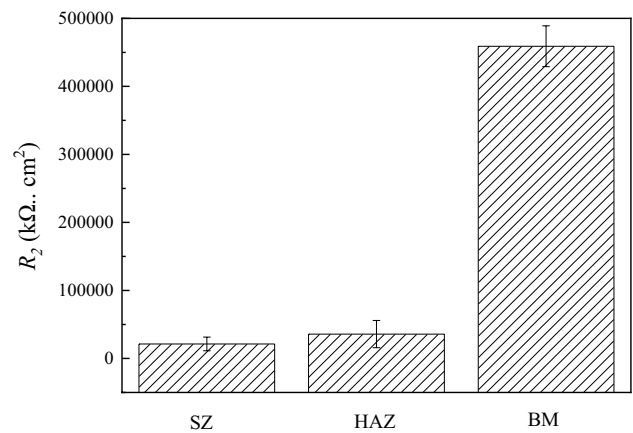


Fig. 10 The variation of film resistance (R_2) of the SZ, HAZ, and BM obtained from Nyquist plots

is shown in Fig. 10. A higher value of R_2 is related to the reduced damage of the oxide film by the chloride of the electrolyte. It can be seen in Fig. 10 that R_2 increases from the SZ, to the HAZ and then further to the BM, with the BM exhibiting the best corrosion performance, and the corrosion resistance of the HAZ being better than that of the SZ.

Figure 11 shows the Bode plots and phase angle diagrams of the three specimens. The values of phase angles are constant and similar with the SZ, HAZ, and BM for the low frequency range of 0.01–1 Hz. The impedance and phase angle values of the BM are much higher than those of the SZ and HAZ for frequencies. In the case of high frequency spectra, of 10^3 to 10^5 Hz, the value of phase angle decreases. It is also clear from Fig. 11 that resistance to electrolyte of the HAZ is higher than that of the SZ.

In every case, the local corrosion performance in a joint is related to microstructural changes. The BM is usually

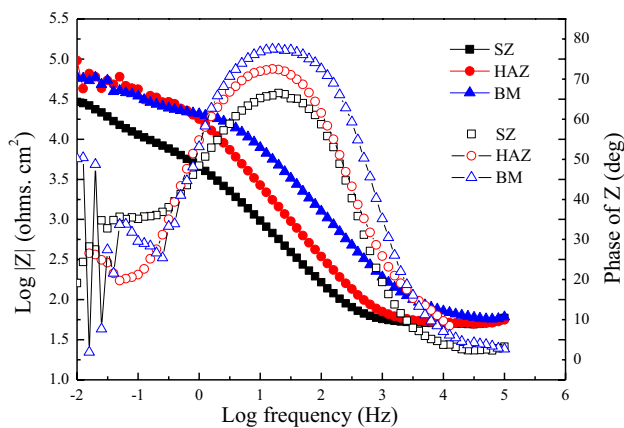


Fig. 11 Bode plot (solid symbols) and phase angle (empty symbols) diagram of the SZ, HAZ, and BM in a 3.5-wt% NaCl solution

clad with pure Al film to improve its corrosion resistance [35]. In the SZ, severe plastic deformation and intense heat input contribute to the formation of diffuse precipitation and coarsening of the S phase, which results further nucleation of pitting corrosion [28]. Furthermore, the SZ has undergone severest plastic deformation during welding. Thus, the size of intermetallics in SZ is smallest and the number is most among BM and HAZ. However, the lower

temperature in HAZ effectively prevents the formation precipitation and coarsening of S-type phase [29, 36, 37].

3.5 Morphology of corrosion attack

Figure 12 shows the SEM micrographs of SZ, HAZ, and BM after the potentiodynamic polarization tests in a 3.5-wt% NaCl solution. In the SZ (Fig. 12a), more pitting holes were found which were formed by combining a large number of smaller pits. It should be noted that a large number of white corrosion products were observed on the surface of SZ. Figure 12b shows a typical pit of the HA, whose depth and numbers of them are lower than those of the SZ. A few pits, which are shallow and small and not connected to other corrosion holes or grooves, can be observed in the HAZ. In addition, there are few pits in the BM and most of the surface has not been unaffected by corrosion (Fig. 12c). The SEM micrographs show that the corrosion severity degree increased in the order $SZ > HAZ > BM$, which is in agreement with the observation from the electrochemical tests. This is related to the size and distribution state of S-phase (Al_2CuMg) and residual impurity particles.

The potential of the S phase is more negative than that of the matrix due to the activity of Mg in the S phase, making the S phase the first to be corroded followed by the

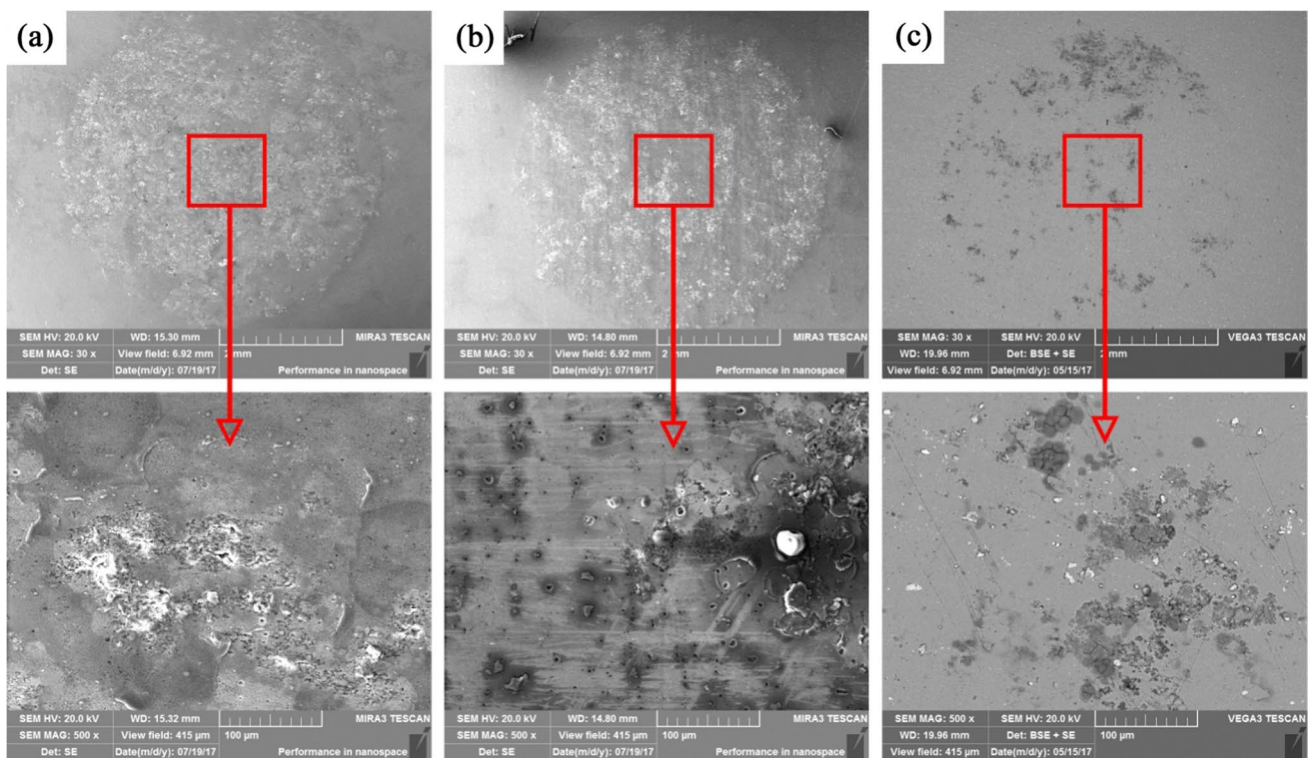


Fig. 12 Corrosion morphology of (a) SZ, (b) HAZ, and (c) BM after performing a Tafel polarization test in 3.5 wt% NaCl solution

creation of pits [28]. In the SZ, the S phase is smaller and it is more uniform, which is associated with increased pit nucleation than the HAZ and BM. Moreover, the refined grains in the SZ would likely decrease corrosion resistance when the dissolution rate is over $10 \mu\text{A}/\text{cm}^2$ [37]. Therefore, the corrosion resistance of the SZ is hindered considerably, compared to the HAZ and BM. All these points are in agreement with morphologies shown in the SEM and the electrochemical test results.

4 Conclusions

In this study, the welding of AA 2024-T3 with FSW was performed at a tool rotational speed of 600 rpm and welding speed of 200 mm/min. The microstructural characteristics, mechanical properties, and corrosion performance were investigated. The findings of the present work can be briefly summarized:

1. A sound joint was produced. The dissolution of the GPB zones in the HAZ is lower than that in the SZ. The SZ shows the smallest grain size and the most disperse intermetallic particles than anywhere in the joint.
2. The hardness in SZ and HAZ was lower than that in the BM. In addition, the lowest hardness of the joint is located at the HAZ due to reduced dissolution of GPB zones and grain size. The fracture location of the joint was located in the HAZ of the RS where the lowest hardness values were measured.
3. From the electrochemical tests and observations of the corrosion attack morphologies, SZ shows the worst corrosion resistance performance between SZ, HAZ, and BM due to the refined grains and a larger number of intermetallic particles during welding. The BM shows the best corrosion resistance.

Funding Financial support was received through the fund of SAST (SAST2016043), the National Key Research and Development Program of China (2016YFB0701203), the China Postdoctoral Science Foundation Funded Project (2020M683558), and the Science and Technology Research Plan of Shaanxi Provincial Education Department (20JK0581).

Data availability The datasets generated during and/or analyzed during the current study are available from the corresponding author on reasonable request.

Declarations

Conflict of interest The authors declare no competing interests.

References

1. Zhang ZH, Li WY, Feng Y et al (2014) Improving mechanical properties of friction stir welded AA2024-T3 joints by using a composite backplate. *Mater Sci Eng A* 598(6):312–318
2. Lu YX, Jing HG, Han YD et al (2016) Numerical modeling of weld joint corrosion. *J Mater Eng Perform* 25(3):960–965
3. Lu YX, Jing HG, Han YD et al (2016) Recommend design of filler metal to minimize carbon steel weld metal preferential corrosion in CO_2 -saturated oilfield produced water. *Appl Surf Sci* 389:609–622
4. Niu PL, Li WY, Zhang ZH et al (2017) Global and local constitutive behaviors of friction stir welded AA2024 joints. *J Mater Sci Technol* 9:987–990
5. Yue YM, Li ZW, Ji SD et al (2016) Effect of reverse-threaded pin on mechanical properties of friction stir lap welded alclad 2024 aluminum alloy. *J Mater Sci Technol* 32(7):671–675
6. Barooni O, Abbasi M, Givi M et al (2017) New method to improve the microstructure and mechanical properties of joint obtained using FSW. *Int J Adv Manuf Tech* 93:4371–4378
7. Aliha MRM, Shahheidari M, Bisadi M et al (2016) Mechanical and metallurgical properties of dissimilar aa6061-t6 and aa7277-t6 joint made by FSW technique. *Int J Adv Manuf Tech* 86(9–12):2551–2565
8. Kang J, Fu RD, Luan GH et al (2010) In-situ investigation on the pitting corrosion behavior of friction stir welded joint of AA2024-T3 aluminium alloy. *Corros Sci* 52(2):620–626
9. Jariyaboon M, Davenport AJ, Ambat R et al (2009) The effect of cryogenic CO_2 cooling on corrosion behaviour of friction stir welded AA2024-T351. *Corros Eng Sci Technol* 44(6):425–432
10. Bayazid SM, Farhangi H, Asgharzadeh H et al (2016) Effect of cyclic solution treatment on microstructure and mechanical properties of friction stir welded 7075 al alloy. *Mater Sci Eng A* 649:293–300
11. Chen S, Zhou Y, Xue J et al (2017) High rotation speed friction stir welding for 2014 aluminum alloy thin sheets. *J Mater Eng Perform* 26(3):1337–1345
12. Imam M, Sun YF, Fujii H et al (2017) Microstructural characteristics and mechanical properties of friction stir welded thick 5083 aluminum alloy. *Metall Mater Trans A* 48(1):208–229
13. Su JQ, Nelson TW, Mishra R et al (2003) Microstructural investigation of friction stir welded 7050–T651 aluminium. *Acta Mater* 51(3):713–729
14. Zhang ZH, Li WY, Li JL et al (2015) Microstructure and anisotropic mechanical behavior of friction stir welded AA2024 alloy sheets. *Mater Charact* 107:112–118
15. Sutton AM, Yang BC, Reynolds AP et al (2004) Banded microstructure in 2024–T351 and 2524–T351 aluminum friction stir welds, Part II Mechanical characterization. *Mater Sci Eng A* 364:66–74
16. Omar H (2008) Effects of peening on mechanical properties in friction stir welded 2195 aluminum alloy joints. *Mater Sci Eng A* 492(1–2):168–176
17. Prime MB, Thomas GH, Baumann JA et al (2006) Residual stress measurements in a thick, dissimilar aluminum alloy friction stir weld. *Acta Mater* 54(15):4013–4021
18. Linton VM, Ripley MI (2008) Influence of time on residual stresses in friction stir welds in agehardenable 7xxx aluminium alloys. *Acta Mater* 56(16):4319–4327
19. Jariyaboon M, Davenport AJ, Ambat R et al (2013) Corrosion of a dissimilar friction stir weld joining aluminium alloys AA2024 and AA7010. *Corros Eng Sci Technol* 41(2):135–142
20. Kamp N, Sullivan A, Robson JD (2007) Modelling of friction stir welding of 7xxx aluminium alloys. *Mater Sci Eng A* 466(1–2):246–255

21. Jariyaboon M, Davenport AJ, Ambat R et al (2007) The effect of welding parameters on the corrosion behaviour of friction stir welded AA2024-T351. *Corros Sci* 49(2):877–909
22. Xu WF, Liu JH (2009) Microstructure and pitting corrosion of friction stir welded joints in 2219-O aluminum alloy thick plate. *Corros Sci* 51(11):2743–2751
23. Zhao ZX, Liang HM, Zhao Y et al (2018) Effect of exchanging advancing and retreating side materials on mechanical properties and electrochemical corrosion resistance of dissimilar 6013-T4 and 7003 aluminum alloys FSW joints. *J Mater Eng Perform* 27(4):1777–1783
24. Kalita SJ (2011) Microstructure and corrosion properties of diode laser melted friction stir weld of aluminum alloy 2024–T351. *Appl Surf Sci* 257(9):3985–3997
25. Li WY, Jiang RR, Huang CJ et al (2015) Effect of cold sprayed Al coating on mechanical property and corrosion behavior of friction stir welded AA2024-T351 joint. *Mater Des* 65:757–761
26. Ma ZY, Feng AH, Chen DL et al (2018) Recent advances in friction stir welding/processing of aluminum alloys: microstructural evolution and mechanical properties. *Crit Rev Solid State Mater Sci* 43(4):269–333
27. Niu PL, Li WY, Li N et al (2019) Exfoliation corrosion of friction stir welded dissimilar 2024-to-7075 aluminum alloys. *Mater Charact* 147:93–100
28. Li N, Li WY, Yang XW et al (2017) Corrosion performance and mechanical properties of friction stir welded AA2024-T3 joints under different corrosion solution exposure. *Mater Corros* 68(9):970–976
29. Bousquet E, Poulon-Quintin A, Puiggali M et al (2011) Relationship between microstructure, microhardness and corrosion sensitivity of an AA 2024–T3 friction stir welded joint. *Corros Sci* 53(9):3026–3034
30. İlevbare GO, Schneider O, Kelly RG et al (2004) In situ confocal laser scanning microscopy of AA 2024–T3 corrosion metrology. *J Electrochem Soc* 151:453–464
31. İpekoğlu G, Erim S, Çam G (2014) Effects of temper condition and post weld heat treatment on the microstructure and mechanical properties of friction stir butt-welded AA7075 Al alloy plates. *Int J Adv Manuf Tech* 70(1–4):201–213
32. Çam G (2012) Investigation of the effect of temper condition on friction stir weldability of AA7075 Al-alloy plates. *Mater Technol* 46(6):627–632
33. Zhang Z, Xiao BL, Ma ZY (2014) Hardness recovery mechanism in the heat-affected zone during long-term natural aging and its influence on the mechanical properties and fracture behavior of friction stir welded 2024Al-T351 joints. *Acta Mater* 73:227–239
34. Genevois C, Deschamps A, Denquin A et al (2006) Quantitative investigation of precipitation and mechanical behaviour for AA2024 friction stir welds. *Acta Mater* 53(8):2447–2458
35. Hu ZL, Wang XS, Yuan SJ (2012) Quantitative investigation of the tensile plastic deformation characteristic and microstructure for friction stir welded 2024 aluminum alloy. *Mater Charact* 73(11):114–123
36. Dixit V, Mishra RS, Lederich RJ et al (2009) Influence of process parameters on microstructural evolution and mechanical properties in friction stirred Al-2024 (T3) alloy. *Sci Technol Weld Joining* 14(4):346–355
37. Ralston KD, Birbilis N, Davies CHJ (2010) Revealing the relationship between grain size and corrosion rate of metals. *Scr Mater* 63:1201–1204

Publisher's note Springer Nature remains neutral with regard to jurisdictional claims in published maps and institutional affiliations.